UNIVERSITY OF LEEDS

This is a repository copy of *Mathematical Model of the Oxidation of a Uranium Carbide Fuel Pellet Including an Adherent Product Layer*.

White Rose Research Online URL for this paper:
http://eprints.whiterose.ac.uk/110903/

Version: Accepted Version

Article:
Shepherd, JS, Fairweather, M, Hanson, BC orcid.org/0000-0002-1720-1656 et al. (1 more author) (2017) Mathematical Model of the Oxidation of a Uranium Carbide Fuel Pellet Including an Adherent Product Layer. Applied Mathematical Modelling, 45. pp. 784-801. ISSN 0307-904X

https://doi.org/10.1016/j.apm.2017.01.041

© 2017 Elsevier Inc. This manuscript version is made available under the CC-BY-NC-ND 4.0 license http://creativecommons.org/licenses/by-nc-nd/4.0/

Reuse
Unless indicated otherwise, fulltext items are protected by copyright with all rights reserved. The copyright exception in section 29 of the Copyright, Designs and Patents Act 1988 allows the making of a single copy solely for the purpose of non-commercial research or private study within the limits of fair dealing. The publisher or other rights-holder may allow further reproduction and re-use of this version - refer to the White Rose Research Online record for this item. Where records identify the publisher as the copyright holder, users can verify any specific terms of use on the publisher's website.

Takedown
If you consider content in White Rose Research Online to be in breach of UK law, please notify us by emailing eprints@whiterose.ac.uk including the URL of the record and the reason for the withdrawal request.

White Rose university consortium
Universities of Leeds, Sheffield & York

eprints@whiterose.ac.uk
https://eprints.whiterose.ac.uk/

Accepted Manuscript

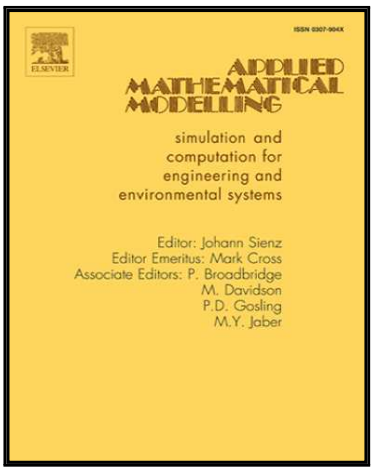

Mathematical Model of the Oxidation of a Uranium Carbide Fuel Pellet Including an Adherent Product Layer

J.S. Shepherd, M. Fairweather, B.C. Hanson, P.J. Heggs

PII: S0307-904X(17)30047-1
DOI: 10.1016/j.apm.2017.01.041
Reference: APM 11539

To appear in: *Applied Mathematical Modelling*

Received date: 4 June 2015
Revised date: 9 January 2017
Accepted date: 12 January 2017

Please cite this article as: J.S. Shepherd, M. Fairweather, B.C. Hanson, P.J. Heggs, Mathematical Model of the Oxidation of a Uranium Carbide Fuel Pellet Including an Adherent Product Layer, *Applied Mathematical Modelling* (2017), doi: 10.1016/j.apm.2017.01.041

This is a PDF file of an unedited manuscript that has been accepted for publication. As a service to our customers we are providing this early version of the manuscript. The manuscript will undergo copyediting, typesetting, and review of the resulting proof before it is published in its final form. Please note that during the production process errors may be discovered which could affect the content, and all legal disclaimers that apply to the journal pertain.

ACCEPTED MANUSCRIPT

Highlights

- Model of the oxidation of UC including an adherent U_3O_8 product layer is presented.
- Highly non-linear numerical solution to a double moving boundary problem.
- Transient heat and mass transfer in expanding oxide and shrinking carbide phases
- Temperature and oxygen concentration sensitivities tested and recommendations made.

ACCEPTED MANUSCRIPT

ACCEPTED MANUSCRIPT

Mathematical Model of the Oxidation of a Uranium Carbide Fuel Pellet Including an Adherent Product Layer

J. S. Shepherd*, M. Fairweather, B. C. Hanson, P. J. Heggs

School of Chemical and Process Engineering, The University of Leeds, Leeds, LS2 9JT, UK

Abstract

Uranium carbide is a candidate fuel for Generation IV nuclear reactors. However, like any candidate fuel, a reprocessing route should be established before implementation. One proposed method involves a pre-oxidation step, where the carbide fuel is oxidised to an oxide and then reprocessed as normal. A mathematical model has been developed to simulate such an oxidation using finite difference approximations of the heat and mass transfer processes occurring. Available literature was consulted to provide coefficients for the reaction rates and importantly the diffusion of oxygen through the adherent oxide layer that forms on the carbide: the rate limiting step. The transient temperature, oxygen and carbon monoxide distributions through the system are modelled in order to predict oxidation completion times and the temperatures reached. It was found that for a spherical pellet of radius 0.935 cm, the oxidation can take between 1 h to 19 h depending on the oxidation conditions and reach temperatures of up to 1556°C. A robust model results that offers increased understanding of a process crucial to the sustainable use of carbide fuels in energy generation.

Keywords: Uranium carbide, Diffusion, Oxidation, Finite difference methods, Moving boundary problem

ACCEPTED MANUSCRIPT

*Corresponding author
Email address: jamesshepherd413@gmail.com (J. S. Shepherd)

ACCEPTED MANUSCRIPT

Nomenclature

Symbols

A	Surface area of the uranium carbide pellet	m
a	Pore size	m
C	Concentration	$\mathrm{mol\,m^{-3}}$
C^B	Concentration in the bulk gas	$\mathrm{mol\,m^{-3}}$
c_p	Specific heat capacity	$\mathrm{J\,kg^{-1}\,K^{-1}}$
D	Diffusivity	$\mathrm{m^2\,s^{-1}}$
$\mathcal{D}_K$	Knudsen diffusivity	$\mathrm{m^2\,s^{-1}}$
d_e	Spherical pellet diameter	m
E_A	Activation energy of uranium carbide oxidation	$\mathrm{J\,mol^{-1}}$
E_A^+	Activation energy of oxygen diffusion through the oxide layer	$\mathrm{J\,mol^{-1}}$
E_{CO}	Activation energy of carbon monoxide oxidation	$\mathrm{J\,mol^{-1}}$
h	Heat transfer coefficient	$\mathrm{W\,m^{-2}\,K^{-1}}$
i	An integer representing the radial node	
k	Thermal conductivity, or an integer representing the radial node at the solid surface	$\mathrm{W\,m^{-1}\,K^{-1}}$
k_1	Rate coefficient for UC oxidation	$\mathrm{m\,s^{-1}}$
k_g	External diffusion coefficient	$\mathrm{m\,s^{-1}}$
L	Cylindrical pellet length	m
$L_{(U)(C,O)}$	Solubility of oxygen in uranium carbide	$\mathrm{J\,mol^{-1}}$
M	Molar mass	$\mathrm{kg\,mol^{-1}}$
n	An integer designating the current time step	
Nu	Nusselt number	
n_{UC}	Number of moles of uranium carbide	mol
$n_{U_3O_8}$	Number of moles of triuranium octoxide	mol
Pr	Prandtl number	
p	An integer representing the radial node at the reaction interface	
r	Radius within solid	m
R	Gas constant	$\mathrm{J\,mol^{-1}\,K^{-1}}$
R_C^*	Rate of oxygen transfer across gas film layer	$\mathrm{mol\,s^{-1}}$
r_{ox}	Radial thickness of the initial layer	m
R_C	Rate of oxygen consumed by UC oxidation	$\mathrm{mol\,s^{-1}}$
R_{CO}	Rate of carbon monoxide oxidation	$\mathrm{mol\,s^{-1}}$
Re	Reynolds number	
r_1	Radius of the carbide pellet	m
r_2	Radius of the solid	m
Sc	Schmidt number	
Sh	Sherwood number	
t	Time passed since reaction started	s
T	Solid temperature	K
T_{Amb}	Ambient temperature	K
T^B	Bulk gas temperature	K
$\bar{T}$	Average temperature	K
u_1, u_2, u_3	Solutions at increment sizes of h_1, h_2 and h_3 respectively	
u	Estimated solution using an infinitely small increment size	
V	Volume of oxidising gas	$\mathrm{m^3}$
v	Coefficient representing $1 - 1/i$	

ACCEPTED MANUSCRIPT

w	Coefficient representing $1 + 1/i$	

Greek symbols

α	Thermal diffusivity	$\mathrm{m^2\,s^{-1}}$
ΔH_R	Enthalpy of oxidation at carbide surface	$\mathrm{J\,mol^{-1}}$
ΔH_{CO}	Enthalpy of carbon monoxide	$\mathrm{J\,mol^{-1}}$
Δr	Radial increment size	m
ε	Emissivity	
μ	Fluid dynamic viscosity	$\mathrm{kg\,m^{-3}}$
μ_{O_2}	Oxygen potential	$\mathrm{J\,mol^{-1}}$
ρ	Density	$\mathrm{kg\,m^{-3}}$
$\dot{\rho}$	Molar density	$\mathrm{mol\,m^{-3}}$
σ	Stefan Boltzmann constant	$\mathrm{W\,m^{-2}\,K^{-1}}$

Subscripts

CO	Carbon monoxide
$fluid$	Oxidising fluid surrounding the pellet
g	Refers either to O_2 or CO
H_2O	Water vapour
m	Represents either UC or U_3O_8 depending on the region under consideration
O_2	Oxygen
UC	Uranium carbide
UO_2	Uranium dioxide
U_3O_8	Triuranium octoxide

Superscripts

n	An integer representing the time step

ACCEPTED MANUSCRIPT

ACCEPTED MANUSCRIPT

1. Introduction

Uranium monocarbide (UC) is under consideration for use in Generation IV reactors due to its higher conductivity and metal atom density making it easier to control in a reactor [12, 11, 3, 19]. An important consideration when implementing a novel fuel type into the nuclear fuel cycle is that it must be able to be efficiently reprocessed. Ideally, carbide fuel would be reprocessed in the same manner as the current most widely used fuel, uranium oxide, in order to save on infrastructure and having to develop new expertise.

A complication arises upon dissolution of carbides in nitric acid, a step in the Purex process currently employed to reprocess oxide fuel. A significant quantity of the carbon displaced by the oxidation remains in the solution as soluble organics, which then reduce the extractability of the fissile material, uranium and plutonium, from the dissolution liquor. This leads to unacceptable losses of fissile material that could otherwise be reused, increasing the volume of nuclear waste generated by carbide fuels.

One proposed solution is pre-oxidising the UC fuel pellet in air to its oxide form allowing reprocessing as normal. The oxidation, however, is highly exothermic making the process potentially dangerous [1, 12]. The motivation of this work, therefore, is to provide a model simulating the oxidation in order to predict the temperature, reaction rate and the occurrence of any dangerous thermal runway under different conditions. This would then help to outline safe operation conditions for the oxidation and help to draw together understanding of UC oxidation into one mathematical description.

As noted in a study of the oxidation completed by Mazaudier *et al.* [12], empirical data for the oxidation of UC is scarce making validation of the completed model difficult. However, this work will help progress the understanding of the reaction through thoroughly modelling the physical processes and coupling this framework to the best possible existing kinetic parameters. Future data on the oxidation can then be input into this model to refine and validate the kinetic constants, facilitating a clear and important progression in understanding the reprocessing of carbide fuels.

The existing literature does include some kinetic parameters presented by Scott [18] in a model describing the burning of graphite uranium fuel in oxygen that are of use, including an Arrhenius expression for the reaction rate. Mukerjee *et al.* [13] added more detail by studying the initiation temperatures and temperature evolution under different oxygen partial pressures during the oxidation of UC microspheres. Although the data are very specific to the UC sample used by Mukerjee *et al.*, they provide a useful comparison for thermal predictions made in this work. The effect of temperature on the reaction has also been studied by Peakall and Antill [15], who provide data on the reaction rate as weight gain of the oxidation of UC compacts at temperatures between 350 °C and 1000 °C. Dell and Wheeler [5] provided data on the effect temperature has on the oxidation of powdered UC completion percentage as well as some observations on the initiation temperature of the reaction with a view to defining the physical factors affecting the oxidation. So whilst not applicable to the oxidation of a spherical pellet, as is considered in this work, their findings were useful in elucidating what physical factors needed to be included in the present model.

The reaction mechanism of the oxidation of air in UC, however, is quite well defined in the literature and is generally thought of as separate oxidations of the uranium and the carbon. The uranium is usually oxidised to U_3O_8 via an intermediate UO_2 phase provided a sufficiently high temperature exists [1, 15, 12, 5]. This temperature can be as low as 250°C, as suggested by the data shown in Table 1 from experiments carried out by Berthinier *et al.* [1] on oxidising UC powder in air. Berthinier *et al.* [1] subjected a crucible containing UC powder to a steady heating ramp, shutting the temperature down at different stages for different runs to examine the phases present at a particular temperature. The carbon is oxidised to CO and then further oxidised to CO_2 provided enough O_2 is present in the gaseous medium surrounding the pellet.

The observations made by Berthinier *et al.* [1] lead to the suggested reaction mechanism below, which is based on the mechanism observed by Borchardt [2] for stoichiometric UC:

$$2UC + 3O_2 \rightarrow 2UO_2 + 2CO \tag{1}$$

$$3UO_2 + O_2 \rightarrow U_3O_8 \tag{2}$$

$$2CO + O_2 \rightarrow 2CO_2 \tag{3}$$

Whilst this mechanism may be viewed as simplified due to the likely presence of other uranium oxides (U_3O_7, for example), it is sufficiently elaborate to represent the significant reactions occurring.

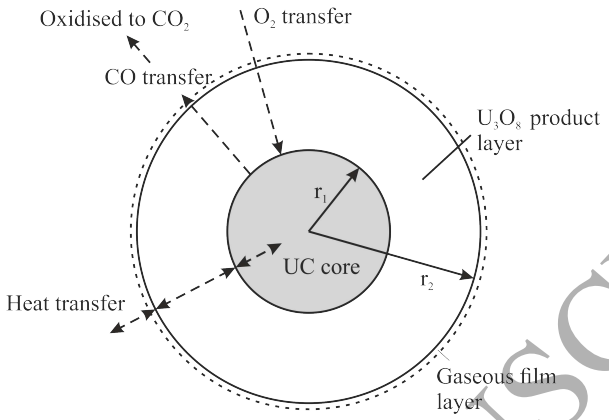

Figure 1: A representation of the oxidation reaction in one dimension with an adherent oxide layer present. Mass and heat transfer through the gaseous film and the oxide layer are considered, as well as how both the carbide and oxide change in size over time.

Shut down temperature (°C)	Ignition temperature (°C)	Phases present
170	none	**UC**
200	195	**UC**+U_3O_8+UO_{2+x}+U_3O_7
250	187	UC+**U_3O_8**+UO_{2+x}+U_3O_7
390	203	**U_3O_8**+UO_{2+x}+U_3O_7
430	170	**U_3O_8**
500	223	**U_3O_8**

Table 1: Reaction products present after the oxidation of UC powder when the temperature ramp is stopped at different stages [1]. The emboldened phase forms the majority.

ACCEPTED MANUSCRIPT

ACCEPTED MANUSCRIPT

An important consideration that follows given this reaction mechanism is whether the oxide product adheres to the surface or spalls off. If the intermediate UO_2 phase immediately spalls from the reaction surface of the pellet, then the further oxidation of UO_2 to U_3O_8 takes place in the surrounding space away from the solid system. This situation has been recently investigated [19, 20] and the time to completely oxidise a spherical pellet of 0 935cm was between 3 h to 30 h depending on the oxidation conditions with temperatures reaching as high as 1458°C. This model develops the work presented by Shepherd *et. al* [20] by including the presence of an adherent oxide layer and the significant effect it has on gaseous mass transfer and hence reaction rate, allowing predictions to be made for a much broader range of oxidation conditions .

However, if the UO_2 does not spall off from the pellet surface, it is quickly oxidised to U_3O_8 and a permanent layer of this material adheres to the pellet. Thus the oxidation of the UC is slower than for the case where the UO_2 spalls due to the diffusion of the reactant O_2 through the adherent layer. This diffusion of O_2 is generally the rate controlling step for the oxidation reaction [13].

As mentioned, it will be assumed that the intermediate UO_2 oxide formed is further oxidised to U_3O_8 significantly faster than it is produced. In other words, the reaction in Eq. 2 occurs significantly faster than the reaction Eq. 1. This assumption is made primarily due to the O_2 availability at the two sites: any O_2 diffusing from the bulk gas through the product layer to the UC surface will have to pass through the UO_2 region, where a significant quantity will be consumed.

The model, therefore, will consider the reactions occurring in Eqs. 1 to 2 to be expressed as an overall equation written as Eq. 4, and the product layer will be assumed to comprise only U_3O_8, as illustrated in Figure 1.

$$3UC + 5.5UO_2 \rightarrow U_3O_8 + 3CO \tag{4}$$

The reaction described by Eq. 4 is taken to be occurring at the surface of the carbide where $r = r_1$ as illustrated in Figure 1, requiring the assumption of a non-porous carbide pellet. The oxidation of CO to CO_2, Eq. 3, will be assumed to be taking place in the bulk gas.

2. Mathematical Representation

The oxidation of the uranium carbide pellet can be represented by a set of equations describing the heat and mass transfer processes involved, the reaction kinetics and the resulting changes in dimension of the solid system.

The model can be separated into distinct sections that require solving at each time step, n:

1. Heat and mass transfer across an external gas film around the pellet.
2. Heat flow through the solid system (both the oxide layer and the carbide).
3. Mass transfer of O_2 and CO in opposite directions through the oxide layer.
4. The resulting reaction rate and heat generated at the UC-U_3O_8 interface.
5. The resulting depletion and reduction in size of the carbide pellet and at the same time the expansion of the U_3O_8 layer.

An illustration of how the spherical pellet changes shape between two instances of time is included in Figure 2.

Before these processes are described, the geometry of the pellet will be characterised. The pellet is assumed to be the equivalent volume sphere of a cylindrical fuel pellet. Its diameter can be calculated using Eq. 5.

$$d_e = 6D/\left[2D/L + 4\right] \tag{5}$$

where d_e is the diameter of the equivalent volume sphere and D and L are the diameter and length of the cylinder it is representing.

The reaction kinetics for the oxidation described in Eq. 1 taking place at the surface of the carbide pellet are provided by Scott [18] and given in Eq. 6:

$$R_C = k_1 exp\left(E_A/R\,T|_{r_1}\right) A_{UC}\; C_{O_2}|_{r_1} \tag{6}$$

ACCEPTED MANUSCRIPT

where R_C is the rate of O_2 consumed by the reaction, k_1 is a constant provided by Scott [18] as $2.0 \times 10^4 \mathrm{g\,mol\,cm^{-2}\,s^{-1}atm^{-1}}$, E_A is the activation energy reported to be $7000\,\mathrm{J\,mol^{-1}}$ [14], R_g the ideal gas constant, A_{UC} is the surface area of the carbide and $T|_{r_1}$ and $C_{O_2}|_{r_1}$ are the temperature and O_2 concentration at the carbide surface, respectively.

2.1. Heat and Mass Transfer

In order to calculate the reaction rate in Eq. 6, it is necessary to know the distribution of heat and O_2 concentration throughout the solid. The methods used in this calculation are presented in this section.

For the general heat transfer through the solid, the Fourier equation for heat conduction in a one dimensional sphere is used.

For $t \geq 0$ and $0 \leq r \leq r_1(t) \leq r_2(t)$:

$$\frac{\partial T_m}{\partial t} = \alpha_m \left(\frac{\partial^2 T_m}{\partial r^2} + \frac{2}{r} \frac{\partial T_m}{\partial r} \right) \tag{7}$$

where $r_1(t)$ is the radius of the reacting carbide, $r_2(t)$ is the radius of the carbide and adherent oxide layer, m designates whether the oxide layer or carbide pellet is under consideration and α is the thermal diffusivity.

$$\begin{aligned} &\text{For } 0 \leq r < r_1(t) && : \quad m = UC \\ &\text{For } r_1(t) \leq r \leq r_2(t) && : \quad m = U_3O_8 \end{aligned}$$

The diffusion of O_2 and CO through the product layer are similarly represented by Fick's second law. Note that the range doesn't include the carbide region, $r < r_1(t)$, as it is assumed to be non-porous.

For $t \geq 0$ and $r_1(t) \leq r \leq r_2(t)$:

$$\frac{\partial C_g}{\partial t} = D_g \left(\frac{\partial^2 C_g}{\partial r^2} + \frac{2}{r} \frac{\partial C_g}{\partial r} \right) \tag{8}$$

where C_g is the concentration, g designates whether O_2 or CO is being considered and D_g is the effective diffusivity of O_2/CO through the product layer.

For the diffusivity of O_2 through the U_3O_8 product layer, D_{O_2}, a value is provided by Jeong *et al.* [9] given in Eq. 9. Jeong *et al.* [9] determined the diffusivity from oxidising UO_2, where the rate limiting step is also the diffusion of O_2 through a U_3O_8 product layer.

$$D_{O_2} = D^+_{O_2} exp\left(-\frac{E^+_A}{R\bar{T}_{U_3O_8}} \right) \tag{9}$$

where $D^+_{O_2}$ is a constant with a value of 1.71×10^{-5}m [9], E^+_A is the activation enthalpy for the diffusion of O_2 through U_3O_8 with a value of $1.6\mathrm{kJ\,mol^{-1}}$ [9] and $\bar{T}_{U_3O_8}$ is the average temperature within the oxide product layer.

For the diffusivity of CO through the product layer, D_{CO}, Knudsen diffusion is assumed. Assuming that Knudsen diffusion is the dominant diffusion mechanism means that the vast majority of particle collisions take place between the diffusing CO molecules and the walls of the pores present in the oxide product [22]. This occurs when the mean free path of the diffusing molecules is comparable to the pore length, and is in contrast to Fickian diffusion where most of the collisions are molecule-molecule which generally occurs at higher pressures. The Knudsen diffusivity is defined, in $\mathrm{cm\,s^{-1}}$, by Smith as [22]:

$$1 \times 10^4 D_{CO} = (\mathcal{D}_K)_{CO} = 9.70 \times 10^3 a \left(\frac{\bar{T}_{U_3O_8}}{M_{CO}} \right)^{\frac{1}{2}} \tag{10}$$

where a is the pore size of the oxide layer in cm, M_{CO} is the molecular weight of CO in $\mathrm{g\,mol^{-1}}$ and $\mathcal{D}_{KCO}$ is the Knudsen diffusivity in $\mathrm{cm^2}$. To obtain the diffusivity of CO, therefore, the Knudsen diffusivity is converted into $\mathrm{m^2\,s^{-1}}$ simply by dividing by a factor of 1×10^4.

ACCEPTED MANUSCRIPT

The initial conditions for Eqs. 7 and 8 are:
For $t \leq 0$:

$$r_1(0) = r_2(0) - r_{ox} > 0 \tag{11}$$

For $t \leq 0$ and $0 \leq r \leq r_2(t)$:

$$T_m = T_{Amb} \tag{12}$$

For $t \leq 0$ and $r_1(t) \leq r \leq r_2(t)$:

$$C_g = 0 \tag{13}$$

where r_{ox} represents a very thin oxide layer present at the beginning of the reaction. This is an assumption made to allow computational times to be significantly shortened. T_{Amb} is the ambient temperature.

There are three positions in the solid where boundary conditions must be applied to Eq. 7: the centre of the solid, the interface between the oxide and the carbide, and the solid surface. For Eq. 8, only the latter two conditions are required.

The heat transfer boundary condition at the centre of the system is adiabatic due to the symmetry of the system.
For $t \geq 0$ and $r = 0$:

$$\left.\frac{\partial T_{UC}}{\partial r}\right|_0 = 0 \tag{14}$$

At the reaction interface, where $r = r_1(t)$, the boundary conditions must allow for the heat generated, O_2 consumed and CO produced by the oxidation. Intimate thermal contact between the carbide and the oxide is assumed as stated in Eq. 15.

Fick's first law is applied for the mass transfer boundary conditions. Given the assumption of Knudsen diffusion for the CO within the U_3O_8 layer, the diffusion coefficient at the interface is taken to be the bulk diffusion of either O_2 through CO or vice-versa occurring within the pores of the product layer. The O_2 transfer boundary condition also includes the solubility of O_2 in UC to represent O_2 loss into the carbide.
For $t \geq 0$ and $r = r_1(t)$:

$$T_{UC} = T_{U_3O_8} \tag{15}$$

$$-k_{UC}\left.\frac{\partial T_{UC}}{\partial r}\right|_{r_1} - \frac{\Delta H_R R_C}{A_{UC}} = -k_{U_3O_8}\left.\frac{\partial T_{U_3O_8}}{\partial r}\right|_{r_1} \tag{16}$$

$$D_{O_2-CO}\left.\frac{\partial C_{O_2}}{\partial r}\right|_{r_1} = \frac{R_C}{A_{UC}}\frac{L_{(U)(C,O)}|_{r_1}}{R\,T_{U_3O_8}|_{r_1}} \tag{17}$$

$$D_{CO-O_2}\left.\frac{\partial C_{CO}}{\partial r}\right|_{r_1} = -\frac{6R_C}{11A_{UC}} \tag{18}$$

where $k_{U_3O_8}$ is the thermal conductivity of U_3O_8, provided by Pillai *et al.* [16], ΔH_R is the enthalpy of the oxidation reaction, D_{g-g} is the bulk diffusivity of one gaseous species, g, through another and $L_{(U)(C,O)}$ is the solubility of O_2 in UC. The factor of 11/6 included in Eq. 18 stems from the stoichiometry of Eq. 4 where 11 moles of O_2 consumed by the reaction produces 6 moles of CO at the carbide surface.

The O_2 solubility in UC is given by Guéneau *et al.* [7] and can be written as:

$$L_{(U)(C,O)} = 30000 - 79T \tag{19}$$

At the solid surface, where $r = r_2(t)$, the boundary conditions represent the transfer of heat and mass from the solid to the bulk gas and vice versa. Due to the assumption of an oxide layer being present from

ACCEPTED MANUSCRIPT

$t = 0$, the surface boundary conditions use variables relevant to U_3O_8. For the O_2 boundary condition at the solid surface, a modified version of Fick's first law is used to include the effect of oxygen chemical potential on its diffusion.

For $t \geq 0$ and $r = r_2(t)$:

$$-k_{U_3O_8} \left.\frac{\partial T_{U_3O_8}}{\partial r}\right|_{r_2} = h\left(T_{U_3O_8}|_{r_2} - T^B\right) + \epsilon_{U_3O_8}\sigma\left(T_{U_3O_8}|_{r_2}^4 - \left(T^B\right)^4\right) \tag{20}$$

$$-D_{O_2-CO} \left.\frac{\partial C_{O_2}}{\partial r}\right|_{r_2} = \frac{\mu_{O_2}|_{r_2}}{R\,T_{U_3O_8}|_{r_2}} k_g\left(C_{O_2}|_{r_2} - C_{O_2}^B\right) \tag{21}$$

$$-D_{CO-O_2} \left.\frac{\partial C_{CO}}{\partial r}\right|_{r_2} = k_g\left(C_{CO}|_{r_2} - C_{CO}^B\right) \tag{22}$$

where h is the heat transfer coefficient, $\epsilon_{U_3O_8}$ is the emissivity of U_3O_8, σ is the Stefan-Boltzmann constant, k_g and C_g^B are the external diffusion coefficient and bulk gas concentration of the gaseous species represented by g, either O_2 or CO, T^B is the temperature of the bulk gas and μ_{O_2} is the oxygen chemical potential in the oxide layer.

The heat transfer coefficient, h, is calculated from the Nusselt number according to Eq. 23:

$$h = \frac{k_{fluid}\mathrm{Nu}}{2r_1} \tag{23}$$

where k_{fluid} is the thermal conductivity of the fluid (air) surrounding the pellet and Nu is the Nusselt number. The Nusselt number is obtained from the Ranz and Marshall [17] correlation, given below:

$$\mathrm{Nu} = 2.0 + 0.6\mathrm{Re}^{1/2}\mathrm{Pr}^{1/3} \tag{24}$$

where Re is the Reynolds number and Pr is the Prandtl number, calculated from Eq. 25:

$$\mathrm{Pr} = \frac{\mu c_{p_{fluid}}}{k_{fluid}} \tag{25}$$

where μ and $c_{p_{fluid}}$ are the dynamic viscosity and specific heat capacity of the fluid, respectively.

A temperature dependent fit of the chemical potential of O_2 in diphasic UO_{2+x}/U_3O_{8-z}, μ_{O_2}, is given by Labroche *et al.* [10]. Labroche *et al.* present a comprehensive review of oxygen potentials in a number of uranium oxides and note that data for monophasic U_3O_8 is sparse, leading to the assumption that the potential in the UO_{2+x}/U_3O_{8-z} phase constitutes the best alternative. It is expressed first as a partial pressure [10]:

$$log(pO_2) = 30.954\left(\frac{1000}{T_{U_3O_8}}\right)^2 - 61.118\left(\frac{1000}{T_{U_3O_8}}\right) + 23.889 \tag{26}$$

where p_{O_2} is the partial pressure of O_2 in UO_{2+x}/U_3O_{8-z}. Partial pressure can then be converted into the oxygen potential as follows:

$$\mu_{O_2} = R_g T_{U_3O_8} ln(pO_2) \tag{27}$$

Due to difficulties in finding any published values for the emissivity of U_3O_8 it was assumed to have the same value as that of UO_2. A value for the total emissivity of UO_2 (the emissivity integrated over all wavelengths) is provided by Geelhood *et al.* [6]:

$$\epsilon_{U_3O_8} \approx \epsilon_{UO_2} = 0.78557 + 1.5263 \times 10^{-5}\, T_{U_3O_8}|_{r_1} \tag{28}$$

ACCEPTED MANUSCRIPT

The external diffusion coefficients represented by k_g control the rate of diffusion of O_2 and CO across the external gas film layer, assumed to comprise CO, surrounding the pellet to the solid surface:

$$k_g = \frac{D_{g-CO}\mathrm{Sh}}{2r_1} \tag{29}$$

where Sh is the Sherwood number. The Sherwood number, similarly to the Nusselt number, can also be expressed via the Ranz and Marshall correlation [17]:

$$\mathrm{Sh} = 2.0 + 0.6\mathrm{Re}^{1/2}\mathrm{Sc}^{1/3} \tag{30}$$

where Sc is the Schmidt number. This is calculated as:

$$\mathrm{Sc} = \frac{\mu}{\rho_{fluid} D_{g-CO}} \tag{31}$$

where ρ_{fluid} is the density of the fluid.

2.2. Calculating the Changing Pellet Size

The above heat and mass transfer calculations allow $T_{U_3O_8}|_{r_1}$ and $C_{O_2}|_{r_1}$ to be known over time. This allows a calculation of the reaction rate provided by Scott [18] in Eq. 6 giving the rate of O_2 consumed. Combining this with the stoichiometry of Eq. 4 gives both the rate of UC depletion and the rate of U_3O_8production.

For $t \geq 0$:

$$\frac{\mathrm{d}n_{UC}}{\mathrm{d}t} = -\frac{6R_C}{11} = -\frac{6k_1 \exp\left(-E_A/R\, T_{U_3O_8}|_{r_1}\right) A_{UC}\, C_{O_2}|_{r_1}}{11} \tag{32}$$

$$\frac{\mathrm{d}n_{U_3O_8}}{\mathrm{d}t} = \frac{2R_C}{11} = \frac{2k_1 \exp\left(-E_A/R\, T_{U_3O_8}|_{r_1}\right) A_{UC}\, C_{O_2}|_{r_1}}{11} \tag{33}$$

where $n_{U_3O_8}$ is the number of moles of U_3O_8. Again, stoichiometric factors are included as R_C represents the moles of U_3O_8 consumed.

The rate of change in the number of moles of each species can be converted to show how the radius of the carbide pellet depletes and the overall solid expands, due to the density decrease from UC to U_3O_8, over time as follows:

For $t \geq 0$:

$$\frac{\mathrm{d}r_1}{\mathrm{d}t} = -\frac{6k_1 \exp\left(-E_A/R\, T_{U_3O_8}|_{r_1}\right) k_g\, C_{O_2}|_{r_1}}{11\dot{\rho}_{UC}} \tag{34}$$

$$\frac{\mathrm{d}r_2}{\mathrm{d}t} = \frac{2k_1 \exp\left(-E_A/R\, T_{U_3O_8}|_{r_1}\right) r_1^2 A_{U_3O_8}\, C_{O_2}|_{r_1}}{11 r_2^2} \left(\frac{1}{\dot{\rho}_{U_3O_8}} - \frac{1}{\dot{\rho}_{UC}}\right) \tag{35}$$

where $\dot{\rho}_{UC}$ and $\dot{\rho}_{U_3O_8}$ are the molar densities of UC and U_3O_8 respectively.

Eqs. 34 and 35 also highlight the non-linearity of this model, given that both r_1 and r_2 are time dependent.

2.3. Oxidation of Carbon Monoxide

The secondary oxidation of CO in the bulk gas is modelled using Eq. 36 given by Howard *et al.* [8]:

$$-\frac{\mathrm{d}C_{CO}^B}{\mathrm{d}t} = 1.3 \times 10^{14} C_{CO}^B \left(C_{O_2}^B\right)^{0.5} \left(C_{H_2O}^B\right)^{0.5} exp\left(-\frac{E_{CO}}{RT^B}\right) \tag{36}$$

where $C_{H_2O}^B$ is the concentration of water vapour in the bulk gas and E_{CO} is the activation energy given as 30kcalmol^{-1} [8], converted to 1.256×10^5J mol^{-1}.

ACCEPTED MANUSCRIPT

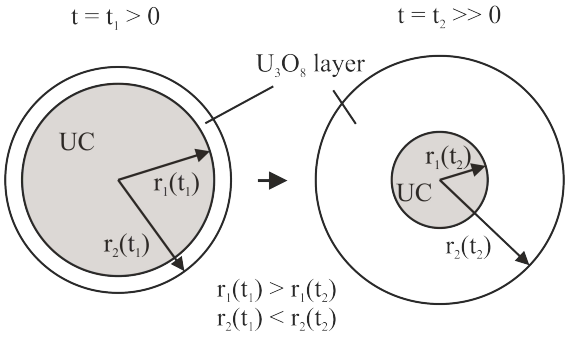

Figure 2: The changing shape of the pellet over time. Over the time interval $\Delta t = t_2 - t_1$, the carbide radius, r_1, decreases while the overall radius of the solid, r_2, increases due to U_3O_8 having a lower density than UC.

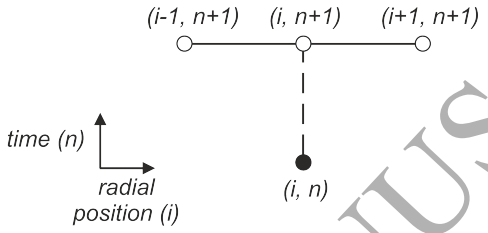

Figure 3: The fully implicit backward method. A known value, at a position i and a time step n, coloured black, is used to find values for the next time step $n+1$, coloured white, at three radial positions $i-1$, i and $i+1$.

This provides a rate of CO depletion in $\mathrm{mol\,mL^{-1}\,s^{-1}}$ which is converted to $\mathrm{mol\,s^{-1}}$ by multiplying by the total volume of oxidising gas, V. CO_2 production can be calculated using the stoichiometry of Eq. 3, as can O_2 when combined with the effects of Eq. 6. The rate of CO oxidation in $\mathrm{mol\,s^{-1}}$ is given as:

$$R_{CO} = -1.3 \times 10^{14} C^B_{CO} \left(C^B_{O_2}\right)^{0.5} \left(C^B_{H_2O}\right)^{0.5} exp\left(-\frac{E_{CO}}{RT^B}\right) V \tag{37}$$

The rate of oxidation of CO given in Eq. 36, when combined with a calculated reaction enthalpy of ΔH_{CO} =-283 $\mathrm{kJ\,mol^{-1}}$for Eq. 3, can be used to predict the resulting change in bulk gas temperature. Assuming that the only thermal effects acting on the bulk gas are convective heat exchange with the pellet and heat generated by the oxidation of CO, and that the gas is well mixed so that the oxidation occurs throughout, the following expression can be used to describe its change in temperature over time:

$$\frac{\mathrm{d}T^B}{\mathrm{d}t} = \frac{1}{\rho_{fluid} c_{p_{fluid}} V} \left(hA\left(T_{U_3O_8}|_{r_2} - T^B\right) + \Delta H_{CO} R_{CO}\right) \tag{38}$$

3. Numerical Solution

The set of equations detailed in Section 2 are solved using a finite difference method know as the fully implicit backward method (FIB) [21], illustrated in Figure 3. The FIB method calculates a solution at three different radial points for the next time step, $n+1$, using just a single known value from the current time step n.

In the case of Eq. 7, the solution is complicated by the need to solve across two solid species that are changing in size differently. In order to model the shrinking carbide and expanding oxide, the radial increment sizes across each, Δr_{UC} and $\Delta r_{U_3O_8}$, are allowed to change whilst the number of radial increments across each is held constant. A FIB approximation of Eq. 7, therefore, must be considered across two different regions.

ACCEPTED MANUSCRIPT

For $n \geq 0$, $2 \leq i \leq p-1$ and $p+1 \leq i \leq k-1$:

$$\frac{T_i^{n+1} - T_i^n}{\Delta t} = \alpha_m \left(\frac{v_i T_{i-1}^{n+1} - 2T_i^{n+1} + w_i T_{i+1}^{n+1}}{\Delta r_m^2} \right) \tag{39}$$

where i is an integer representing the radial increment across the solid, $v_i = 1 - 1/i$ and $w_i = 1 + 1/i$. At the solid centre, $i = 1$, at the reaction interface, $i = p$, and at the solid surface, $i = k$.

The radial increment sizes are therefore calculated as:

For $n \geq 0$ and $1 \leq i \leq p-1$:

$$\Delta r_{UC} = \frac{r_1^n}{k-2} \tag{40}$$

For $n \geq 0$ and $p \leq i \leq k$:

$$\Delta r_{U_3O_8} = \frac{r_2^n - r_1^n}{(p-1) - k} \tag{41}$$

The FIB representation of Eq. 8, the mass transfer through the oxide layer, is of the same form as Eq. 39.

For $n \geq 0$ and $k+1 \leq i \leq p$:

$$\frac{(C_g)_i^{n+1} - (C_g)_i^n}{\Delta t} = D_g \left(\frac{v_i (C_g)_{i-1}^{n+1} - 2(C_g)_i^{n+1} + w_i (C_g)_{i+1}^{n+1}}{\Delta r_{U_3O_8}^2} \right) \tag{42}$$

Eqs. 39 and 42 are rearranged in order to organise them into separate tri-diagonal matrices, each requiring a solution at every time step.

For $n \geq 0$ and $2 \leq i \leq p-1$:

$$-M_{UC} v_i T_{i-1}^{n+1} + (1 + 2M_{UC})\, T_i^{n+1} - M_{UC} w_i T_{i+1}^{n+1} = T_i \tag{43}$$

For $n \geq 0$ and $p+1 \leq i \leq k-1$:

$$-M_{U_3O_8} v_i T_{i-1}^{n+1} + (1 + 2M_{U_3O_8}) T_i^{n+1} - M_{U_3O_8} w_i T_{i+1}^{n+1} = T_i^n \tag{44}$$

$$-M_{O_2} v_i (C_{O_2})_{i-1}^{n+1} + (1 + 2M_{O_2})\, (C_{O_2})_i^{n+1} - M_{O_2} w_i (C_{O_2})_{i+1}^{n+1} = (C_{O_2})_i^n \tag{45}$$

$$-M_{CO} v_i (C_{CO})_{i-1}^{n+1} + (1 + 2M_{CO})\, (C_{CO})_i^{n+1} - M_{CO} w_i (C_{CO})_{i+1}^{n+1} = (C_{CO})_i^n \tag{46}$$

where $M_{UC} = \alpha_{UC} \Delta t / \Delta r_{UC}^2$, $M_{U_3O_8} = \alpha_{U_3O_8} \Delta t / \Delta r_{U_3O_8}^2$, $M_{O_2} = D_{O_2} \Delta t / \Delta r_{U_3O_8}^2$ and $M_{CO} = D_{CO} \Delta t / \Delta r_{U_3O_8}^2$.

To complete the tri-diagonal matrices and allow them to be solved, finite difference approximations of the boundary conditions must be included to remove imaginary points that occur outside the domain of Eqs. 43-46. A central difference approximation is used for all following boundary condition approximations due to the FIB approximations of the Fourier equation and Fick's second law being second order.

When considering the boundary condition at the centre of the solid, where $r = 0$, Eq. 7 cannot be applied as the second term on the right hand side is indeterminate as $\partial T / \partial r = 0$ and $r = 0$. Applying L'Hôpital's rule to this term and setting $r = 0$ allows Eq. 7 to be expressed as:

For $t \geq 0$ and $r = 0$:

$$\frac{\partial T_{UC}}{\partial t} = 3\alpha_{UC} \left(\frac{\partial^2 T_{UC}}{\partial r^2} \right) \tag{47}$$

Applying the FIB method to Eq. 47 allows it to be expressed as:

For $n \geq 0$ and $i = 1$:

$$\frac{T_1^{n+1} - T_1^n}{\Delta t} = 3\alpha_{UC} \left(\frac{v_1 T_0^{n+1} - 2T_1^{n+1} + w_1 T_2^{n+1}}{\Delta r_{UC}^2} \right) \tag{48}$$

The problem term in Eq. 48 is T_0^{n+1}, occurring at the imaginary point $i = 0$. In order to allow its removal, a central difference approximation of the heat transfer boundary condition at the centre of the solid is given in Eq. 49.

For $n \geq 0$ and $i = 1$:

$$\frac{T_2^n - T_0^n}{2\Delta r_{UC}} = 0 \tag{49}$$

Eq. 49 therefore allows the removal of the imaginary point, $i = 0$, from Eq. 43 when $i = 1$, resulting in Eq. 43 taking the form of Eq. 50 when $i = 1$.

For $n \geq 0$ and $i = 1$:

$$(1 + 2M_{UC})\, T_1^{n+1} - 2M_{UC} T_2^{n+1} = T_1^n \tag{50}$$

The next set of boundary conditions that require approximating are those at the UC/U_3O_8 interface, represented by Eqs. 16, 17 and 18. For the heat transfer boundary condition, it is necessary to simplify Eq. 16 using the assumption provided in Eq. 15 that there is intimate thermal contact between the two solids. The finite difference approximations of the three boundary conditions at the interface are:

For $n \geq 0$ and $i = p$:

$$\left(\frac{k_{UC}}{\Delta r_{UC}} - \frac{k_{U_3O_8}}{\Delta r_{U_3O_8}}\right) \frac{T_{p-1}^n - T_{p+1}^n}{2\Delta r_{U_3O_8}} = -\Delta H_R k_1 \exp\left(-E_A/RT_p^n\right) (C_{O_2})_p^n \tag{51}$$

$$D_{O_2} \frac{(C_{O_2})_{p-1}^n - (C_{O_2})_{p+1}^n}{2\Delta r_{U_3O_8}} = k_1 \exp\left(-E_A/RT_p^n\right) (C_{O_2})_p^n \frac{L^n_{(U)(C,O)_p}}{RT_p^n} \tag{52}$$

$$D_{CO} \frac{(C_{CO})_{p-1}^n - (C_{CO})_{p+1}^n}{2\Delta r_{U_3O_8}} = -\frac{6}{11} k_1 \exp\left(-E_A/RT_p^n\right) (C_{O_2})_p^n \tag{53}$$

Rearranging Eqs. 51, 52 and 53 for the imaginary values, T_{p-1}^n, $(C_{O_2})_{p-1}^n$ and $(C_{CO})_{p-1}^n$ and substituting into Eqs. 44, 45 and 46 results in the tri-diagonal matrices taking the following forms at $i = p$.

For $n \geq 0$ and $i = p$:

$$\left\{1 + 2M_{U_3O_8} + \frac{2M_{U_3O_8} y_{U_3O_8} \Delta H_R k_1 \exp\left(-E_A/RT_p^{n+1,z}\right) (C_{O_2})_p^{n+1,z})}{T_k^{n+1,z}}\right\} T_k^{n+1,z+1} - 2M_{U_3O_8} T_{p+1}^{n+1,z+1} = T_k^n \tag{54}$$

$$\left\{1 + 2M_{O_2} + \frac{2M_{O_2} y_{O_2} k_1 \exp\left(-E_A/RT_p^{n+1,z}\right) L^n_{(U)(C,O)_p} (C_{O_2})_p^{n+1,z}}{(C_{O_2})_k^{n+1,z} RT_p^{n+1,z}}\right\} (C_{O_2})_k^{n+1,z+1} - 2M_{O_2} (C_{O_2})_{p+1}^{n+1,z+1} = (C_{O_2})_k^n \tag{55}$$

$$\left\{1 + 2M_{CO} + \frac{12M_{CO} y_{CO} k_1 \exp\left(-E_A/RT_p^{n+1,z}\right) (C_{O_2})_p^{n+1,z}}{11(C_{CO})_k^{n+1,z}}\right\} (C_{CO})_k^{n+1,z+1} - 2M_{CO} (C_{CO})_{p+1}^{n+1,z+1} = (C_{CO})_k^n \tag{56}$$

where $y_{U_3O_8} = \Delta r_{U_3O_8} v_p / (k_{UC} - k_{U_3O_8})$, $y_{O_2} = \Delta r_{U_3O_8} v_p / D_{O_2}$ and $y_{CO} = \Delta r_{U_3O_8} v_p / D_{CO}$.

ACCEPTED MANUSCRIPT

ACCEPTED MANUSCRIPT

Here, z represents the number of iterations used to ensure the non-linearity of these boundary conditions does not destabilise the model. This is necessary as solving for T^{n+1} and C_g^{n+1} requires prior knowledge of T_k^{n+1} and $(C_g)_k^{n+1}$, meaning that it is necessary to linearise the relevant equations. For example, Eq. 54 has been linearised by multiplying both the numerator and denominator of the heat of reaction term by T_k^{n+1} allowing it to take the tri-diagonal form shared by Eqs. 43 and 44. The calculation is then iterated a number of times until the tolerances characterised in Eqs. 57 and 58 are satisified.

For the first iteration, it is assumed that $T_k^{n+1} = T_k^n$ and $(C_g)_k^{n+1} = (C_g)_k^n$. The solution is then recalculated at the same time step, n, using the newly calculated values for T_k^{n+1} and $(C_g)_k^{n+1}$:

$$\frac{T_k^{n+1,z+1} - T_k^{n+1,z}}{T_k^{n+1,z+1}} < \text{Tolerance for all temperatures} \tag{57}$$

$$\frac{(C_g)_k^{n+1,z+1} - (C_g)_k^{n+1,z}}{(C_g)_k^{n+1,z+1}} < \text{Tolerance for all concentrations} \tag{58}$$

The final boundary conditions required to complete the matrices are those at the the solid surface, represented by Eqs 20 and 22.

For $n \geq 0$ and $i = k$:

$$\frac{T_{k+1}^n - T_{k-1}^n}{2\Delta r_{U_3O_8}} = -\frac{h^n}{k_{U_3O_8}}(T_k^n - T^B) - \frac{\epsilon\sigma}{k_{U_3O_8}}((T_k^n)^4 - (T^B)^4) \tag{59}$$

$$\frac{(C_{O_2})_{k+1}^n - (C_{O_2})_{k-1}^n}{2\Delta r_{U_3O_8}} = -\frac{k_{O_2}^n \mu_{O_2}^n}{D_{O_2} R T_k^n}\left((C_{O_2})_k^n - (C_{O_2})^B\right) \tag{60}$$

$$\frac{(C_{CO})_{k+1}^n - (C_{CO})_{k-1}^n}{2\Delta r_{U_3O_8}} = -\frac{k_{CO}^n}{D_g}\left((C_{CO})_k^n - (C_{CO})^B\right) \tag{61}$$

Rearranging Eqs. 59 and 61 for the imaginary values, T_{k+1}^n and $(C_g)_{k+1}^n$, and substituting into Eqs. 44, 45 and 46 results in the tri-diagonal matrices taking the following forms at $i = k$.

For $n \geq 0$ and $i = k$:

$$-2M_{U_3O_8}T_{k-1}^{n+1,z+1} + \Bigg\{1 + 2M_{U_3O_8} + 2M_{U_3O_8}u_{U_3O_8} + \frac{2M_{U_3O_8}u_{U_3O_8}}{h^{n+1}}\epsilon\sigma(T_k^{n+1,z})^3 - \frac{2M_{U_3O_8}u_{U_3O_8}T^B}{T_k^{n+1,z}} - \frac{2M_{U_3O_8}u_{U_3O_8}}{h^{n+1}T_k^{n+1,z}}\epsilon\sigma(T^B)^4\Bigg\}T_k^{n+1,z+1} = T_k^n \tag{62}$$

$$-2M_{O_2}(C_{O_2})_{k-1}^{n+1,z+1} + \left\{1 + 2M_{O_2} + 2M_{O_2}u_{O_2} - \frac{2M_{O_2}u_{O_2}\mu_{O_2}^n(C_{O_2})^B}{(C_{O_2})_k^{n+1,z}RT_k^{n+1,z}}\right\}(C_{O_2})_k^{n+1,z+1} = (C_{O_2})_i^n \tag{63}$$

$$-2M_{CO}(C_{CO})_{k-1}^{n+1,z+1} + \left\{1 + 2M_{CO} + 2M_{CO}u_{CO} - \frac{2M_{CO}u_{CO}(C_{CO})^B}{(C_{CO})_k^{n+1,z}}\right\}(C_{CO})_k^{n+1,z+1} = (C_{CO})_i^n \tag{64}$$

ACCEPTED MANUSCRIPT

where $u_{U_3O_8} = \Delta r_{U_3O_8} w_k h / k_{U_3O_8}$, $u_{O_2} = \Delta r_{U_3O_8} w_k k_g^n / D_{O_2}$ and $u_{CO} = \Delta r_{U_3O_8} w_k k_g^n / D_{CO}$.

The equations detailed in this section, therefore, provide the details on how to construct the three tri-diagonal matrices required to solve for: the temperature across the carbide and oxide layer, the concentration of O_2 through the oxide layer and the concentration of CO through the oxide layer. With these quantities now known at each time step, they can be used in backward difference approximations of the radial change equations, Eqs. 34 and 35. For $n \geq 0$:

$$r_1^{n+1} = r_1^n - \frac{\Delta t 6 k_1 \exp\left(-E_A / R T_p^{n+1}\right) (C_{O_2})_p^{n+1} k_g^{n+1}}{11 \dot{\rho}_{UC}} \tag{65}$$

$$r_2^{n+1} = r_2^n - \frac{\Delta t 2 k_1 \exp\left(-E_A / R T_p^{n+1}\right) (C_{O_2})_p^{n+1} (r_1^{n+1})^2}{11 (r_2^{n+1})^2} \left(\frac{1}{\dot{\rho}_{U_3O_8}} - \frac{1}{\dot{\rho}_{UC}} \right) \tag{66}$$

Using Eq. 65, therefore, the radial depletion over time can be calculated and hence the time until the reaction is completed. The simulation finishes when the percentage of carbide oxidised is 99%. It is held from fully completing because as the carbide increment size tends to zero, $\Delta r_{UC} \to 0$, so does the time step size, meaning that to fully oxidise the carbide would take an infinite amount of time. The details of the dependence of the time step size on the radial increment sizes are covered in the next section.

3.1. Ensuring Numerical Stability

The numerical stability of this model was maintained through use of the Courant-Friedrichs-Lewy rule [21]. It requires slight modification however to accommodate the differing radial increment sizes and the thermal and mass diffusivities involved in the solution. In order to maintain stability, the time step must be the smallest value possible from the array of values it can be calculated from. This can be seen in the part-logical, part-mathematical calculation of the time step that is used, given in Eq. 67:

$$\Delta t = \frac{1}{2 MAX\left(\alpha_{UC}, \alpha_{U_3O_8}, D_{O_2}, D_{CO}\right)} MIN\left(\Delta r_{UC}, \Delta r_{U_3O_8}\right) \tag{67}$$

where $MAX()$ represents a function used in the model to select the largest value from the variables listed in the brackets, and $MIN()$ the smallest.

This equation is applied at the beginning of each time step once the relevant variables (increment sizes and diffusivities) have been calculated. Initially it is very small due to the small size of the oxide product layer. It then increases throughout the reaction before decreasing again as the radius of remaining carbide depletes. Despite this restriction slowing the simulation time of the oxidation greatly, it is necessary to ensure stability and confidence in the results.

How the time step size varies over time can be seen in Figure 4. It starts off small due to the thin, initial oxide layer having a small increment size, $\Delta r_{U_3O_8}$, across it and then increases as the product layer grows. Then, approximately midway through the reaction, when Δr_{UC} becomes smaller than $\Delta r_{U_3O_8}$ due to depletion of the carbide, it begins to decrease as Δr_{UC} does. This result was obtained using a carbide pellet with an initial radius of 0.20 cm and a bulk gas with a temperature of 900°C and an O_2 concentration of 3.15 mol m^{-3}.

3.2. Checking for Convergence

Convergence of the model was checked by varying the number of increments across both the carbide and oxide layers whilst maintaining the values of all other parameters. The results of this can be seen in Table 2.

Richardson's deferred approach to the limit [21] was used to extrapolate the results displayed in Table 2 to predict the solution for infinitely small increment sizes. Taking the first three results from Table 2 and applying them to Eqs. 68 and 69 facilitates the prediction of such a solution:

$$u = \frac{h_2^p u_1 - h_1^p u_2}{h_2^p - h_1^p} \tag{68}$$

ACCEPTED MANUSCRIPT

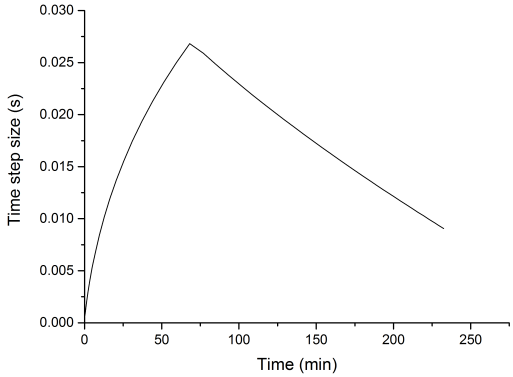

Figure 4: The variation of the time step size over reaction time. The initial increase is due to an expanding increment size of the oxide, $\Delta r_{U_3O_8}$, and the later decrease is due to the shrinking Δr_{UC} becoming dominant in Eq. 67.

Number of Radial Increments Across Carbide	Number of Radial Increments Across Oxide	Oxidation Completion Time (h)	Computational Time (min)
5	5	9.043	0.046
10	10	10.25	0.183
20	20	10.82	0.743
40	40	11.09	2.861
80	80	11.24	12.04

Table 2: The effect of varying the number of increments on the oxidation completion time as a test for convergence for the model with an oxide layer present.

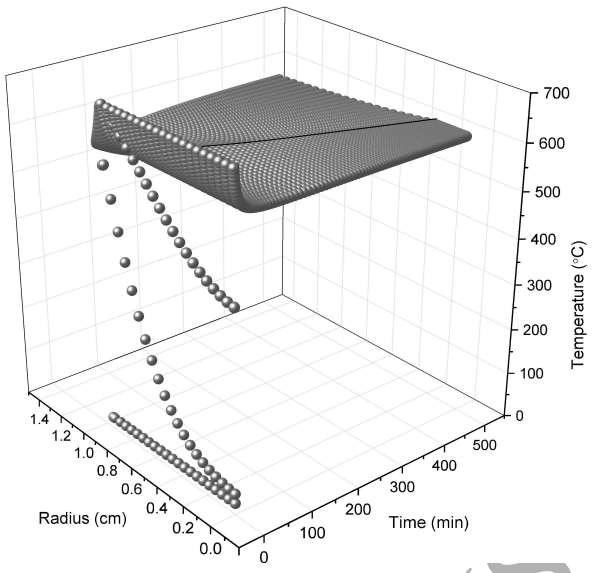

Figure 5: Radial temperature distribution over time illustrating the shrinking carbide in black, the expanding oxide in grey and the thermal response of the solid.

where u_1 and u_2 are the solutions (completion times) at initial radial increment sizes of h_1 and h_2, and p can be calculated from:

$$2^p = \frac{u_2 - u_1}{u_3 - u_2} \tag{69}$$

where u_3 is the solution at h_3, and $h_3 = \frac{1}{2}h_2 = \frac{1}{4}h_1$.

Eqs. 68 and 69 yield a result of u =11.33 h, which combined with the results in Table 2 indicate that the model is converging successfully.

The effect of time step size on the reaction completion time can also be seen from Table 2, as when the number of increments is increased the simulation completion time increases significantly.

4. Results

The model is capable of predicting the reaction completion time, as well as the transient temperature distribution through the solid and the O_2 and CO concentration distributions through the oxide layer. An example of modelling the temperature distribution over time can be seen in Figure 5, and examples of the concentration distributions can be seen in Figures 6 and 7. For these results, a carbide pellet of radius r_1 =0.935 cm was used initially at 25°C and exposed to bulk gas with a volume of 1 m^3 and a temperature held constant at 500°C. The bulk gas O_2 concentration at the beginning of the reaction was 3.15 mol m^{-3}, representing 21% O_2 in air at 1.01 bar, and the CO concentration was assumed to be constant and zero.

Figure 5 displays an initial steep temperature rise in the carbide, shown in black, caused by both the exposure to the hotter bulk gas and the exothermic oxidation. It then peaks and begins to cool down slightly. This is due to the formation of the U_3O_8 oxide layer retarding the initially rapid reaction rate, causing less heat to be generated by the reaction. The temperature throughout the solid then remains largely constant for the remainder of the reaction.

Figure 5 also illustrates the lack of a temperature gradient throughout the carbide due to its high thermal conductivity of $20.4 + 2.836 \times 10^{-6}\,(t - 570)^2$ W cm^{-1} K^{-2} [4] where t is the temperature in °C, in this case taken to be the average temperature of the UC.

Figure 6 highlights the steep O_2 concentration through the product layer. At $r = r_2$, the solid surface, the O_2 concentration approaches the concentration of O_2 in the bulk gas (it remains lower, however, due

ACCEPTED MANUSCRIPT

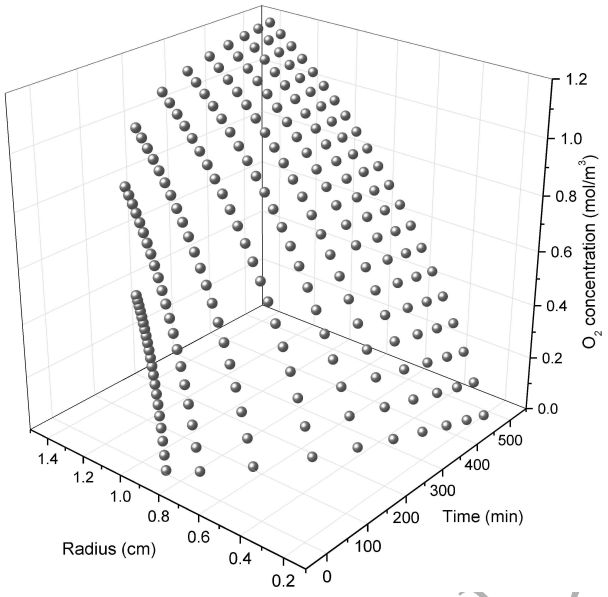

Figure 6: Radial O_2 distribution through the expanding oxide layer over time. The gradient is largely constant with time, and the minimal value at the oxide-carbide interface suggests O_2 diffusion is the rate limiting step.

to it having to diffuse across the external gas film layer). At $r = r_1$, the oxide-carbide interface, the O_2 concentration is essentially zero, with the value at $t = 233\,\text{min}$ being $C_{O_2}|_{r_1} = 4.78 \times 10^{-6}\text{mol}\,\text{m}^{-3}$. This suggests that the O_2 is being consumed by the surface reaction, R_C, significantly faster than it can diffuse from the bulk gas to the reaction site, allowing the conclusion that the reaction rate is limited and controlled by the rate of O_2 diffusion through the product layer, D_{O_2}.

Figure 7 illustrates the similarly steep concentration gradient of CO through the product layer, with the maximum occurring at $r = r_1$ where it is being generated and a minimum at $r = r_2$ where it is lost to the bulk gas, assumed in this case to have a constant value of $C^B_{CO} = 0\,\text{mol}\,\text{m}^{-3}$.

Figures 5, 6 and 7 also allow the expansion of the overall solid to be observed, with the initial solid radius of $r_2 = 0.945\,\text{cm}$ increasing to $r_2 = 1.324\,\text{cm}$.

A closer examination of the O_2 and CO distributions in the oxide layer at a time step late in the reaction, $t = 232.5\,\text{min}$, can be observed in Figure 8.

Sensitivity studies were carried out on the model by varying input parameters to see what effects they have on the oxidation. Figure 9 is a plot of the effect of the bulk gas temperature on the reaction completion time, and Figure 10 plots the effect it has on the temperature at the reaction interface. A carbide pellet of radius 0.935 cm and initial temperature of 25°C was used with an initial O_2 concentration in the bulk gas of $3.15\,\text{mol}\,\text{m}^{-3}$ for all simulations, representing 21% O_2 in $1\,\text{m}^3$ of air at 1.01 bar. An initial CO concentration of zero was assumed as was an initial oxide layer thickness of 0.01 cm. Table 3 quantifies the effects the gas temperature has on the completion time and the maximum interface temperature, which is the position within the solid that reaches the highest temperature.

Figure 9 and Table 3 indicate that increasing the gas temperature greatly reduces the oxidation completion time. Figure 10 demonstrates that the maximum temperature reached in the pellet, occurring at the UC/U_3O_8 interface, also increases significantly with the gas temperature.

Similar sensitivity studies were carried out on the effect of the initial O_2 concentration in the bulk gas with the results presented in Figures 11 and 12. For these results, the bulk gas temperature was 500°C and a carbide pellet with an initial radius and temperature of 0.935 cm and 25°C was assumed. The initial oxide layer present was again assumed to have a thickness of 0.01 cm, and the air pressure was 1.01 bar and its volume $1\,\text{m}^3$.

Figures 11 and 12 and Table 4 illustrate the effect that the O_2 concentration has on the reaction rate. The

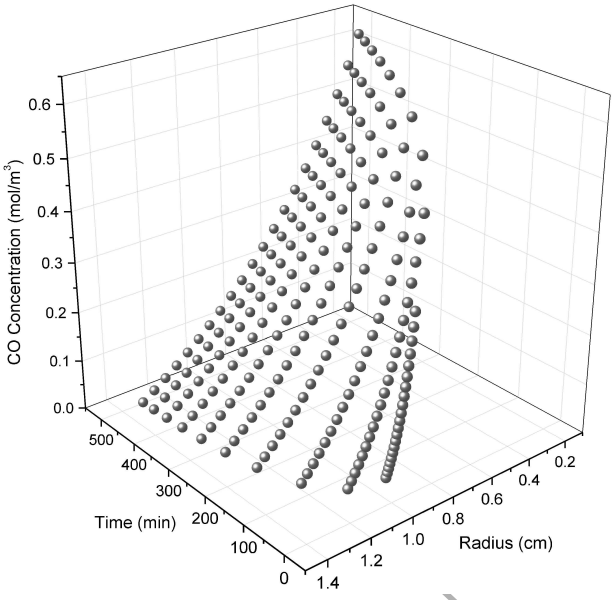

Figure 7: Radial CO distribution through the oxide layer. It is generated at the reaction interface and diffuses out to the bulk gas.

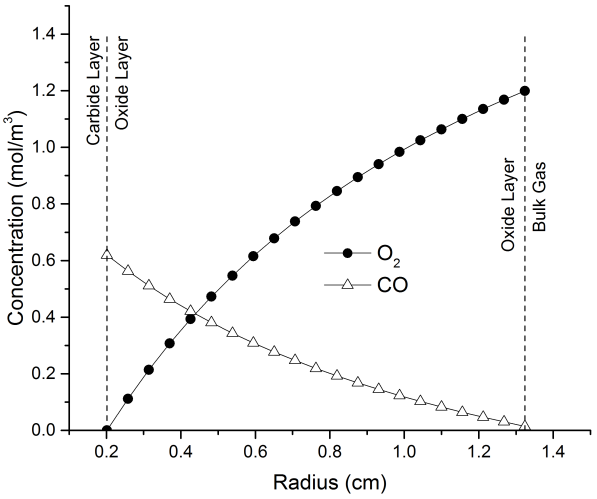

Figure 8: The O_2 and CO distributions through the oxide product layer towards completion of the reaction at $t = 484$ min. At $t = 0$, $r_1 = 0.935$ cm and $r_2 = 0.945$ cm.

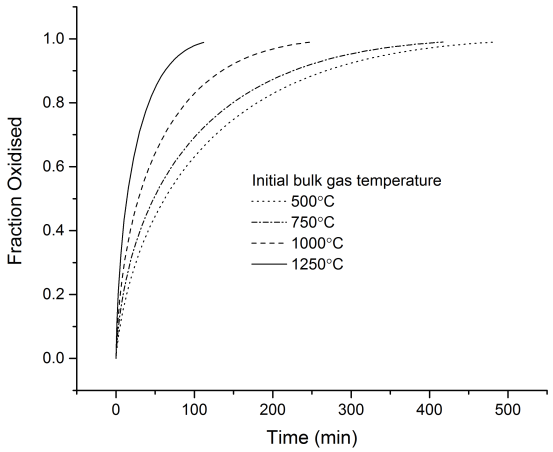

Figure 9: The effect of varying the bulk gas temperature, assumed to be constant, on the completion time of the oxidation reaction.

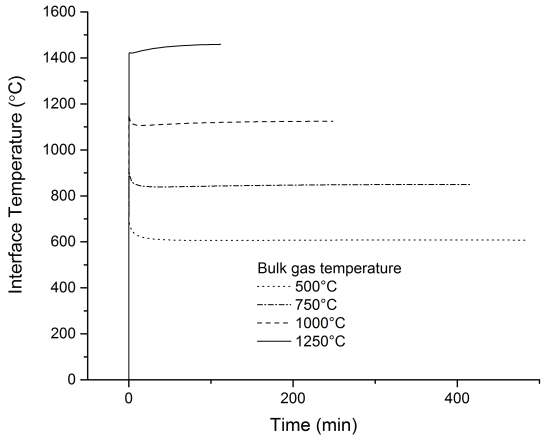

Figure 10: The effect of varying the bulk gas temperature on the temperature at the UC/U_3O_8 interface.

Bulk Gas Temperature, T^B (°C)	Maximum Interface Temperature, $T_{U_3O_8}\|_{r_1}$ (°C)	Reaction Completion Time (h)
500	607	3.922
750	849	2.393
1000	1153	1.633
1250	1458	7.767

Table 3: The dependence of the maximum temperature reached at the UC/U_3O_8 interface and the reaction completion time on the bulk gas concentration.

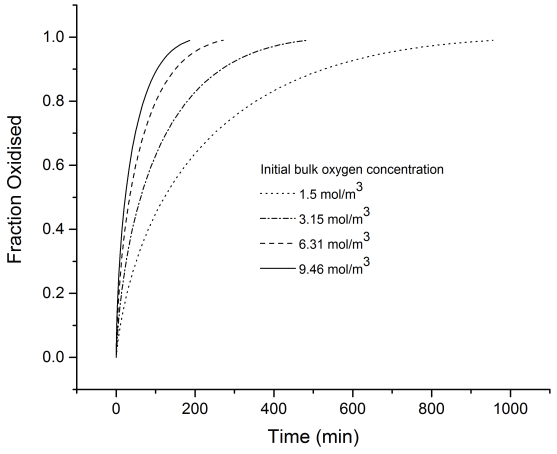

Figure 11: Curves representing fraction of uranium carbide oxidised over time at different initial O_2 concentrations in the bulk gas.

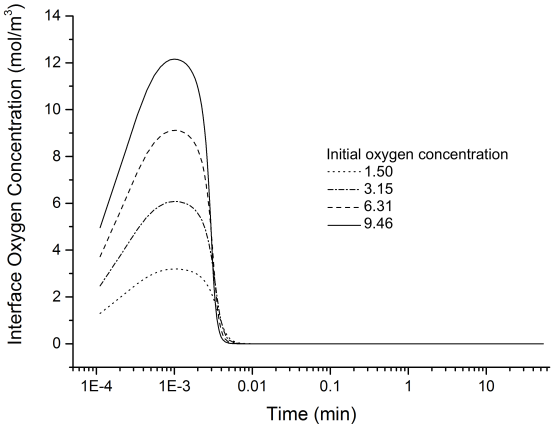

Figure 12: The effect of the bulk O_2 concentration on the O_2 concentration at the reaction interface over time.

ACCEPTED MANUSCRIPT

Bulk Gas Oxygen Concentration, $C^B_{O_2}$ (mol m^{-3})	Maximum Interface Temperature, $T_{U_3O_8}\|_{r_2}$ (K)	Reaction Completion Time (min)
1.50 (10%)	578	956
3.15 (21%)	608	484
6.31 (40%)	653	271
9.46 (60%)	697	186

Table 4: The dependence of the surface and interface temperatures on the bulk gas O_2 concentration, as well as the resulting reaction completion times.

significant increase, and resulting increase in the temperature reached, was expected due to the suggestion that O_2 supply to the reaction is the rate limiting step. Increasing the O_2 concentration to 9.46 mol m^{-3}, for example, reduces the reaction completion time to 186 min compared to the 484 min in air.

Figure 12 is a logarithmic plot included to detail the O_2 concentration at the reaction interface over time. Due to the stated initial conditions, at $t = 0$, $C_{O_2}|_{r_1} = 0$. As O_2 then transfers into the product layer from the bulk gas, the concentration at the interface rises. This allows the oxidation reaction to proceed, which rapidly consumes the O_2. Continuous consumption of O_2 by the oxidation maintains the concentration at the interface as $C_{O_2}|_{r_1} \approx 0$.

5. Conclusions

A transient mathematical model with two moving-boundaries and independent meshes for the oxidation of a UC pellet was developed. An adherent oxide product layer comprising U_3O_8 adheres and expands. Heat transfer through the solid and mass transfer through the U_3O_8 were represented by the Fourier equations at any instant of time, with non-linear boundary conditions at both the interface between the UC and the U_3O_8 and at the solid surface. These boundary conditions are necessary for the processes of heat and mass transfer between the solid and the bulk gas, and for the generation of heat at the reaction interface.

The resulting set of partial and ordinary differential equations were solved numerically through implicit and explicit finite difference approximations. Linearisation of equations such as Eq. 54 at each time step was necessary to account for the high non-linearity. Convergence at each time step was enforced before proceeding to the next increment of time.

The numerical stability of the model was controlled by a dynamic time step size calculated from the Courant-Friedrichs-Lewy condition, which accommodates the change in the size of the radial increment. The numerical solution was checked for convergence by progressively increasing the number of radial increments and using Richardsons deferred appproach to the limit methodology.

The stable model was then able to predict the temperature distribution through the solid and the concentrations of O_2 and CO through the U_3O_8 layer, and use them to predict the reaction completion times and the maximum temperatures reached. For a typical spherical UC pellet with a radius of 0.935 cm, the oxidation takes between 1-8h depending on the input parameters. The maximum temperature reached of 1458°C occurred when a O_2 content of 21% along with a high gas temperature of 1000°C was used. Lower O_2 concentrations and temperatures can be used to bring the maximum temperature down quite significantly, with a peak of 578 °C predicted at 10% O_2 and a gas temperature of 500 °C, suggesting that these parameters could provide safe operating conditions for the oxidation without compromising too much on the completion time.

Comparison of these predictions to those obtained from a model where the U_3O_8 layer does not adhere [20], indicates that the product layer slows the reaction. For example, at 500 °C, 21% O_2 and an initial radius of 0.935 cm, an increase in the reaction completion time from 3.71 h to 3.92 h is predicted. The cause for this increase in the completion time can be attributed to the need for the reacting oxidant to diffuse through the product layer before it reaches the reaction interface. Additionally, the slower reaction rate,

ACCEPTED MANUSCRIPT

especially toward the completion of the reaction as the product layer has thickened, causes the maximum temperature reached to decrease from 1458 °C to 1004 °C when an adherent U_3O_8 layer is considered. The combination of the model presented in this work and that by Shepherd *et al.* [20] therefore allows predictions to be made for both circumstances: where the oxide layer adheres and where it does not.

The model provides an alternative to Scott's model of graphite fuel oxidation [18] in that it considers a U_3O_8 product layer, as is suggested to be the case in practice [1, 15, 12]. It also adds the calculation of the transient O_2 and CO gradients through the product layer while considering the oxygen solubility and potential in U_3O_8 adding an important layer of extra detail as oxygen diffusion is the rate limiting step.

Being able to predict temperatures and reaction times makes the model a useful tool in defining controlled and safe parameters for the processing of UC. No thermal runaway is predicted under the broad temperature and oxygen concentration ranges applied, due to the retarding effect of the adherent oxide layer on the reaction, suggesting that remaining below an operating temperature of 1250 °C is safe. The authors' recommend an operating temperature of 750 °C and an air atmosphere for optimal reaction completion time and energy use, as higher temperatures result in diminishing returns in reducing the reaction duration.

As well as predicting the characteristics of the oxidation, the completed model presents an industrial benefit by providing a better understanding of the oxidation itself. A wide range of literature has been consulted to establish the physical, kinetic and thermal parameters associated with species involved in the reaction. Temperature dependencies, where applicable, have been defined and a detailed mathematical description of the physical processes observed to occur has been provided. Coupled to the robust numerical solution applied to such a description, the model is a valuable tool for investigating UC oxidation conditions and provides an excellent framework for the future fitting of kinetic variables to novel experimental data. Ideally, such data would include temperatures of the carbide and surrounding atmosphere throughout the reaction as well as completion times. Sensitivity to external temperature, oxygen concentration and also the nature of the UC pellet would be valuable in validating the relevant kinetics in this model. Work is ongoing within the same project that supported this work to provide such data, and this will be incorporated in the model described once available. The present model, together with parallel model developments, does, however, allow different promising routes to processing carbides to be assessed, i.e. via direct dissolution in nitric acid with subsequent removal of organics from solution via oxidative techniques, or via a pre-oxidative treatment to convert the carbide fuel to an oxide, and then applying the Purex process. These models are capable of predicting safe operating envelopes for reprocessing carbide fuels, particularly for the oxidation of fuels that are highly exothermic, as well as characterising reaction times and efficiencies. Improvements in their accuracy will accrue as more detailed kinetic data become available.

Using this single pellet oxidation as a foundation, further work will include examining the oxidation using more advanced, three-dimensional approaches to model a batch oxidation due to it being the likeliest implementation of the oxidation in a processing environment.

Acknowledgements

The research leading to the results contained in this paper received funding from the European Union 7th Framework Programme FP7-Fission-2011-2.3.1 under grant agreement number 295825 (Project ASGARD). The paper reflects only the authors views and the European Union is not liable for any use that may be made of the information contained therein.

References

[1] Berthinier, C., Coullomb, S., Rado, C., Le Guyadec, F., Chatillon, C., Blanquet, E., Boichot, R., 2009. Experimental thermal analysis of uranium carbide powder ignition. In: Proceedings of Global 2009. Vol. 6131. pp. 1496–1503.

[2] Borchardt, H., 1959. Observations on reactions of uranium compounds. Journal of Inorganic and Nuclear Chemistry 12 (12), 113 – 121.

[3] Chartier, A., Brutzel, L. V., 2007. Modeling of point defects and rare gas incorporation in uranium mono-carbide. Nuclear Instruments and Methods in Physics Research Section B: Beam Interactions with Materials and Atoms 255 (1), 146 – 150.

[4] De Coninck, R., Van Lierde, W., Gijs, A., 1975. Uranium carbide: Thermal diffusivity, thermal conductivity and spectral emissivity at high temperatures. Journal of Nuclear Materials 57 (1), 69–76.

ACCEPTED MANUSCRIPT

[5] Dell, R., Wheeler, V., 1967. The ignition of uranium mononitride and uranium monocarbide in oxygen. Journal of Nuclear Materials 21 (3), 328 – 336.
[6] Geelhood, K., Luscher, W. G., Beyer, C., 2011. FRAPCON-3.4: A Computer Code for the Calculation of Steady State Thermal-mechanical Behavior of Oxide Fuel Rods for High Burnup. US Nuclear Regulatory Commission, Office of Nuclear Regulatory Research Richland, WA.
[7] Guneau, C., Dupin, N., Sundman, B., Martial, C., Dumas, J.-C., Goss, S., Chatain, S., Bruycker, F. D., Manara, D., Konings, R. J., 2011. Thermodynamic modelling of advanced oxide and carbide nuclear fuels: Description of the upuoc systems. Journal of Nuclear Materials 419 (13), 145 – 167.
[8] Howard, J. B., Williams, G. C., Fine, D. H., 1973. Kinetics of carbon monoxide oxidation in postflame gases. Symposium (International) on Combustion 14 (1), 975–986.
[9] Jeong, S. M., Kwon, K.-C., Park, B. H., Seo, C.-S., 2006. A kinetic study of the oxidation of uranium dioxide. Reaction Kinetics and Catalysis Letters 89 (2), 269–275.
[10] Labroche, D., Dugne, O., Chatillon, C., 2003. Thermodynamics of the o-u system. i - oxygen chemical potential critical assessment in the uo_2-u_3o_8 composition range. Journal of nuclear materials 312 (1), 21–49.
[11] Legand, S., Bouyer, C., Dauvois, V., Casanova, F., Lebeau, D., Lamouroux, C., 2014. Uranium carbide dissolution in nitric acid: speciation of organic compounds. Journal of Radioanalytical and Nuclear Chemistry 302 (1), 27–39.
[12] Mazaudier, F., Tamani, C., Galerie, A., Marc, Y., 2010. On the oxidation of (U, Pu)C fuel: Experimental and kinetic aspects, practical issues. Journal of Nuclear Materials 406 (3), 277–284.
[13] Mukerjee, S. K., Rao, G. A. R., Dehadraya, J. V., Vaidya, V. N., Venugopal, V., Sood, D. D., 1994. The oxidation of uranium monocarbide microspheres. Journal of Nuclear Materials 210 (12), 97–106.
[14] Naito, K., Kamegashira, N., Kondo, T., Takeda, S., 1976. Isothermal oxidation of uranium monocarbide powder under controlled oxygen partial pressures. Journal of Nuclear Science and Technology 13 (5), 260–267.
[15] Peakall, K. A., Antill, J. E., 1962. Oxidation of uranium monocarbide. Journal of the Less Common Metals 4 (5), 426–435.
[16] Pillai, C. G. S., Dua, A. K., Raj, P., 2001. Thermal conductivity of U_3O_8 from 300 to 1100 K. Journal of Nuclear Materials 288 (23), 87–91.
[17] Ranz, W. E., Marshall, W. R., 1952. Evaporation from drops: Part 1. Chemical Engineering Progress 48 (3), 141–146.
[18] Scott, C. D., 1966. Analysis of combustion of graphite-uranium fuels in a fixed bed or moving bed. Industrial & Engineering Chemistry Process Design and Development 5 (3), 223–233.
[19] Shepherd, J. S., 2015. Mathematical modelling of the oxidation and dissolution of uranium carbide. Ph.D. thesis, University of Leeds.
[20] Shepherd, J. S., Fairweather, M., Heggs, P. J., Hanson, B. C., 2015. Mathematical modelling of the pre-oxidation of a uranium carbide fuel pellet. Computers and Chemical Engineering 83 (1), 203–213.
[21] Smith, G. D., 1965. Numerical Solution of Partial Differential Equations. Oxford University Press.
[22] Smith, J. M., 1970. Chemical Engineering Kinetics. McGraw-Hill.

ACCEPTED MANUSCRIPT